11-2012

Ultrasonic Detection Using π-Phase-Shifted Fiber Bragg Gratings

Thomas Fink
University of Nebraska-Lincoln, tfink6@gmail.com

ULTRASONIC DETECTION USING π-PHASE-SHIFTED FIBER BRAGG GRATINGS

by

Thomas D. Fink

A THESIS

Presented to the Faculty of

The Graduate College at the University of Nebraska

In Partial Fulfillment of Requirements

For the Degree of Master of Science

Major: Electrical Engineering

Under the Supervision of Professor Ming Han

Lincoln, Nebraska

November, 2012

ULTRASONIC DETECTION USING π-PHASE-SHIFTED FIBER BRAGG GRATINGS

Thomas Fink, M.S

University of Nebraska, 2012

Advisor: Ming Han

Optical fiber sensors for ultrasonic detection have become a subject of much research in recent years. In this thesis an optical fiber ultrasonic sensor based on a π-phase-shifted fiber Bragg grating (πFBG) is experimentally investigated. Several methods of fabricating πFBGs are investigated for use in this work. The parameters used to characterize the fabricated sensors are discussed. An experimental demodulation setup is developed based on a laser-intensity demodulation scheme. The directivity of a πFBG sensor is experimentally determined to greatly depend upon the impinging angle of the ultrasonic wave. The sensitivity of a πFBG sensor to ultrasonic waves generated by a piezoelectric transducer at various frequencies is experimentally investigated. The response of a πFBG sensor to an ultrasonic acoustic emission simulated by a pencil lead break event is investigated. The noise sources of the system are theoretically analyzed. The parameters of the system affecting the signal-to-noise ratio are theoretically determined.

ACKNOWLEDGEMENTS

First, I would like to thank my advisor, Ming Han, for the opportunity to work on this project. In addition, the guidance he has provided over the last two years has been invaluable. He has helped me to grow as a researcher and provided a path for me to do so.

I would like to thank my thesis review committee, Professor Dennis Alexander and Professor Natale Ianno, for their time in examining my thesis and participating in its review.

I would like to thank the colleagues in my research group Qi Zhang, Tongqing Liu, Fawen Guo, and Jiajun Tian for their advice and assistance. I would furthermore like to thank Qi Zhang for her work helping me with the UV πFBG fabrication setup, Fawen Guo for his work with the CO_2 πFBG fabrication method, and Tongqing Liu for his theoretical work on πFBG ultrasonic detection.

I would sincerely like to show my gratitude to my family, especially my parents, who have been my support over the last seven years. I would also like to thank Samantha Cleary who helped keep me on track, and even helped me prepare my final presentations while I was ill.

This work is supported by the Office of Naval Research under grant number N000141110262.

Table of Contents

Table of Figures

Chapter 1

Introduction

1.1 Motivation

Ultrasonic emission detection is an important part of Structural Health Monitoring (SHM). Many defects in structures emit detectable acoustic ultrasonic waves upon formation, as well as upon deterioration [1-3]. Ultrasonic waves can also be induced into a structure in order to evaluate material integrity, such as in the case of ultrasound based testing [4]. Currently, ultrasonic emission detection is primarily performed with ceramic piezoelectric transducers (PZTs) [2].

Optical fiber based sensors have many desirable qualities that offer advantages over electronic sensors such as PZTs in the field of SHM. Optical fiber is made of durable silica glass, is light weight, and has a small profile. These qualities allow it to be embedded in various structures with minimal effects to structural integrity [5-7]. Such embedded sensors would be able to monitor a structure throughout their lifetime. Due to the non-conductive nature of silica, optical fiber boasts immunity to electromagnetic interference. Many fiber sensors, particularly fiber Bragg grating (FBG) based sensors, also have excellent multiplexing capability [1, 8, 9]. Since a FBG sensor occupies only a

very narrow bandwidth, a distributed sensor array could be easily fabricated by writing many FBG sensors onto a single fiber at different locations.

Partly because of these qualities, FBG based sensors have recently been a subject of much interest for use as ultrasonic sensors [1, 10, 11]. A FBG is shown schematically in Fig. 1.1a. The mechanism of detection for a FBG in most applications relies on observing a shift in its reflection spectrum, which is shown in Fig. 1.1b. In the case of ultrasonic emission detection, the strain of ultrasonic waves impinging upon a FBG sensor causes a spectral shift in its Bragg wavelength. One method of FBG interrogation is by observing laser intensity reflection [12, 13]. This involves locking the wavelength of a narrow-linewidth laser to a linear portion of the FBG reflection spectrum. The spectral shift caused by the strain of ultrasonic waves impinging upon the FBG can then be observed via the reflected laser intensity.

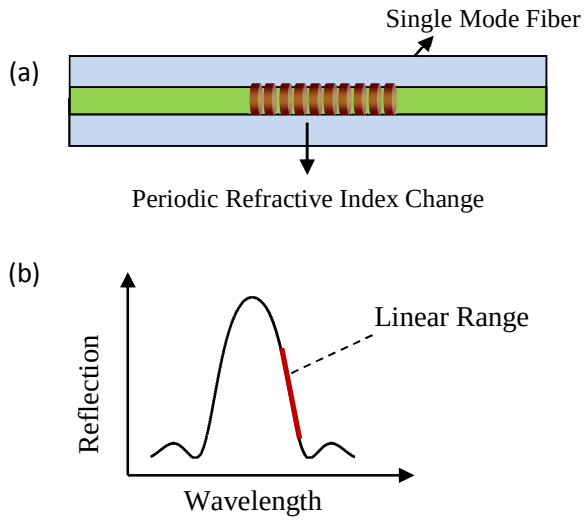

Figure 1.1: Schematic of a FBG (a) and its reflection spectrum (b).

Unfortunately, traditional FBGs have two important areas that require some improvement for ultrasonic emission detection, sensitivity and bandwidth. The width of the typical FBG reflection spectrum (~0.3 nm) leads to relatively shallow spectral slopes. This combined with the short wavelength shift from the low amplitude ultrasonic emissions typically encountered in such sensing applications results in the limited sensitivity of traditional FBG sensors. Ultra-long FBG sensors may theoretically greatly increase the reflectivity and decrease the overall width of the reflection spectrum, thus increasing sensitivity. However, these ultra-long FBG sensors are limited in fabrication because of the high degree of accuracy required to fabricate such a long grating. Furthermore, as the physical wavelength of an ultrasonic wave becomes shorter than the FBG being used to measure it, sensitivity is greatly reduced. So while ultra-long FBG sensors improve sensitivity, they reduce the effective sensing bandwidth.

π-Phase-shifted Fiber Bragg Gratings (πFBG) may provide a solution to the sensitivity problems of the FBG in the case of ultrasonic emission detection[14-17]. A πFBG is a special grating that differs from a FBG by introducing a π-phase-shift at the center of the otherwise periodic grating. This can be thought of as separating a FBG into two separate smaller FBGs. Then this structure can be considered as an in-fiber Fabry-Perot (FP) cavity between two FBG mirrors. If the reflectivity of the πFBG is very high, then this increases the quality factor of the FP cavity. The result of adding a π-phase-shift in the center of a highly reflective FBG is an extremely narrow notch forming in the center of the reflection spectrum. This spectral notch can then be used to facilitate ultrasonic detection in a similar manner to normal FBGs by locking the laser wavelength to the

linear region of the spectral notch and observing the change in reflectivity due to the spectral shift.

1.2 Theoretical Background

A FBG is a distributed in-fiber Bragg reflector, and is structurally just a periodic refractive index change of a certain length in the core of a fiber. A πFBG, shown schematically in Fig. 1.2a, introduces a π-phase-shift at the center of the otherwise periodic structure of a FBG. This leads to a narrow spectral notch in the πFBG's reflection spectrum as shown in Fig. 1.2b.

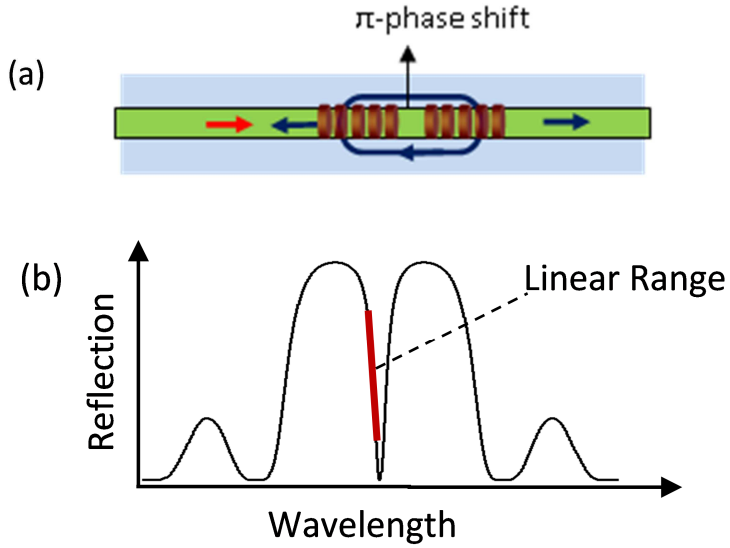

Figure 1.2: Schematic of a πFBG (a) and its reflection spectrum (b).

The position of the spectral notch formed in the πFBG reflection spectrum is located at the Bragg wavelength, given by

$$\lambda_B = 2n_{eff}\Lambda_0 \tag{1.1}$$

where n_{eff} is the effective refractive index for the propagating optical mode of the fiber, and Λ_0 is the period of the periodic refractive index change in the fiber core [18]. From Eq. 1.1 it is seen that a change in the grating period or effective refractive index will result in a spectral shift of the Bragg wavelength.

The strain from ultrasonic waves impinging upon the fiber alters both the effective refractive index, via the elasto-optic effect, as well as the grating period[19, 20]. Thus, these waves can be observed by monitoring the spectral shift of the πFBG. This is accomplished here in a similar fashion to normal FBG sensors by locking the wavelength of a narrow linewidth laser to the linear portion of the spectral notch and observing the change in the reflected laser power.

Since the linear portion of the spectral notch acts as a frequency discriminator, we find that the maximum spectral slope, *k*, is proportional to the signal amplitude when using this method of demodulation. From Fig. 1.3, it is clear that a πFBG has a clear advantage over the FBG in this regard. These slopes are found through numerical simulation of both a πFBG and FBG sensor.

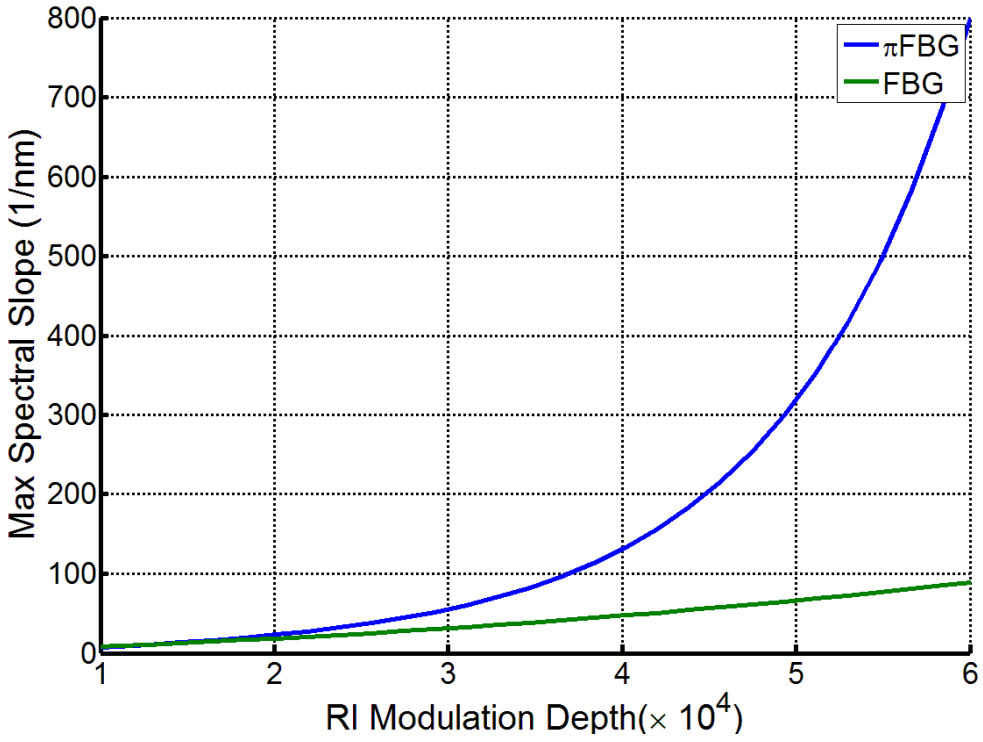

Figure 1.3: Maximum spectral slope, *k*, as a function of the refractive index modulation depth, plotted for both a theoretical πFBG sensor and a theoretical FBG sensor.

1.3 Thesis Organization

The aim of this thesis is ultimately to investigate the experimental response of πFBG based sensors to ultrasonic waves impinging upon them and perform an analytical noise analysis of the experimental system. It is organized as follows:

Chapter 1 contains the motivation of the work and includes a minimal amount of background theory and the organization of this thesis. Chapter 2 discusses the various methods that were developed to fabricate the gratings used for this work. Some useful characterizations for πFBGs are also discussed. Chapter 3 contains the primary experimental work of this thesis. The experimentation and results are discussed in detail.

Chapter 4 contains a noise analysis of the results obtained from experimentation. Chapter 5 provides some summary of this work, and discusses the future of this work.

Chapter 2

Fabrication of πFBGs

2.1 Ultraviolet Phase-Mask Fabrication of FBGs

A FBG is formed by a periodic refractive index change in the core of the fiber. Other works in the past have found a suitable method of FBG fabrication involving an ultraviolet (UV) excimer laser and a phase mask [21].

When UV light of certain wavelengths irradiates photosensitive silica, a change in the refractive index of the silica occurs. The Ge-doped core of standard Single Mode Fiber (SMF) has some inherent photosensitivity to UV light, especially at wavelengths near 193 nm [22]. Experiments have shown that SMF is not sensitive enough to longer wavelengths of UV light to be efficient for highly reflective FBG fabrication[23]. For this reason, an ArF excimer laser operating at 193 nm is used for this work.

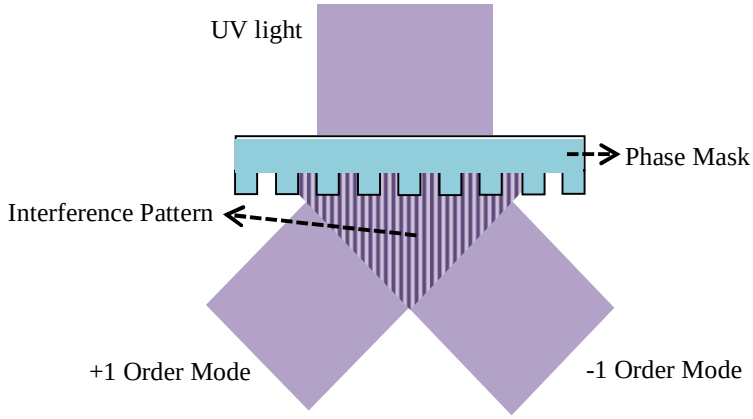

Figure 2.1: Schematic of the optical path of UV light through a phase mask with suppressed 0 order and suppressed higher order modes.

The phase mask is a surface relief grating of a specific period that is etched onto fused silica. For this work, a phase mask is used that suppresses the 0 order modes and high order modes of the interference pattern, leaving only the ±1 order modes. Shining the UV light through the phase mask forms a periodic interference pattern, as shown in Fig. 2.1. By aligning the core of a SMF with the interference pattern, a periodic refractive index change can be achieved in the fiber core.

2.2 CO_2 Pulsed Laser Post-Processing of FBGs

A method for fabricating πFBGs by post-processing of FBGs with a pulsed CO_2 laser was investigated for this work. First, a normal FBG was fabricated using the UV phase-mask method mentioned above. Then the FBG was attached to an apparatus, shown in Fig. 2.2, which applied strain to the grating via a weight. A pulsed CO_2 laser was focused onto the center of the grating. As the center of the grating is heated to a temperature near the melting point of the silica, an elongation in the fiber occurs due to the strain from the weight. By controlling the weight applied to the grating, the laser's

pulse frequency, and the laser's pulse duty cycle, the amount of elongation of the fiber can be controlled.

The reflection spectrum observed during the fabrication process is shown in Fig. 2.2 for several durations of CO_2 laser irradiation. As the fiber is stretched, a dip forms due to the increasing phase shift at the center of the grating. This dip shifts towards the center of the grating, until a π phase shift is achieved. Longer durations of irradiation show that the dip continues to shift past the center wavelength of the grating until it disappears. Even further irradiation shows another dip forming and shifting towards the grating center wavelength, indicating a 3π phase shift has occurred.

Unfortunately, this method had several drawbacks that made it difficult to implement. In order to accurately determine the phase shift created in the fiber, the FBG reflection spectrum must be monitored in real time. Heating the grating induces a large spectral shift, due to the refractive index variations in the fiber due to temperature. In addition, a large amount of optical noise that saturated the reflection spectrum interrogator used to monitor the FBG. Furthermore, heating the center of the grating to a near melting point may introduce structural anomalies in the fiber core, reducing the quality factor of the resulting πFBG.

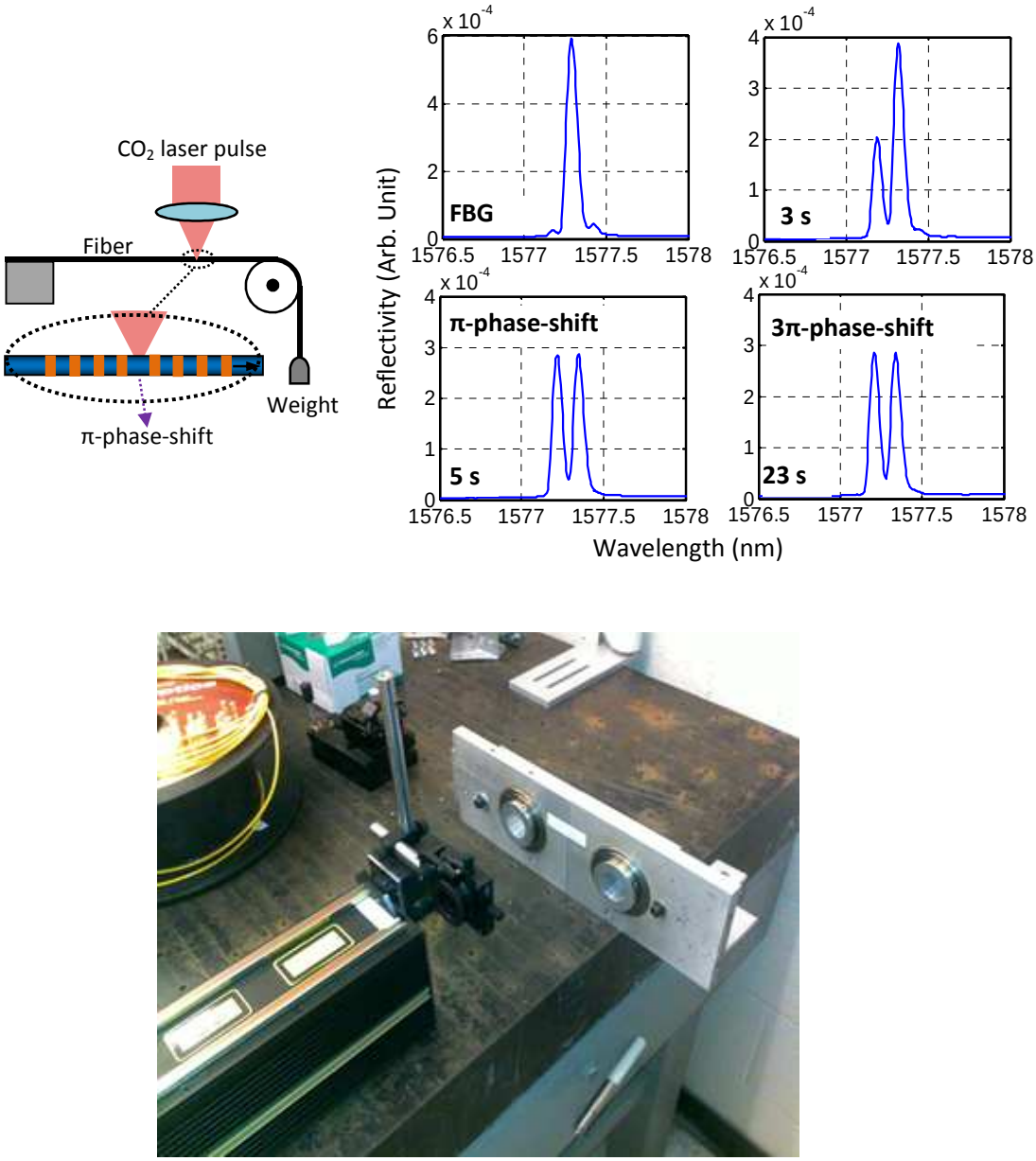

Figure 2.2: Schematic of the πFBG fabrication setup (left), reflection spectrum of the original regular FBG and during the CO2 laser heating process (right), and image of the physical setup (Bottom).

2.3 Ultraviolet Phase-Mask with Inclusion of Nano-Positioning Stage for πFBG fabrication

The primary method used for fabrication of πFBGs for this work is closely based on the UV laser and phase mask method described above. In addition to the components necessary for FBG fabrication, a movable aperture and a nano-positioning stage on which the phase mask is mounted are used for πFBG fabrication. The movable aperture controls the area of the fiber that can be affected by the UV light, and the nano-positioning stage allows the phase mask to be precisely moved during fabrication. Also in this particular setup, the UV laser is scanned across the grating via motorized translation stage in order to ensure a uniform grating reflectivity. This is necessary because the excimer laser used has a Gaussian beam profile. The complete setup used for πFBG fabrication is shown in Fig. 2.3. The method of πFBG fabrication is then as follows: 1) The moveable aperture is adjusted to a position to write half of the grating. 2) The UV laser is scanned across the aperture to write half of the grating. 3) The aperture is moved over the area of the second half of the grating. 4) The phase mask is moved by a distance of half the phase mask period to create a π-phase-shift in the interference pattern. 5) The UV laser is again scanned across the movable aperture to write the second half of the grating.

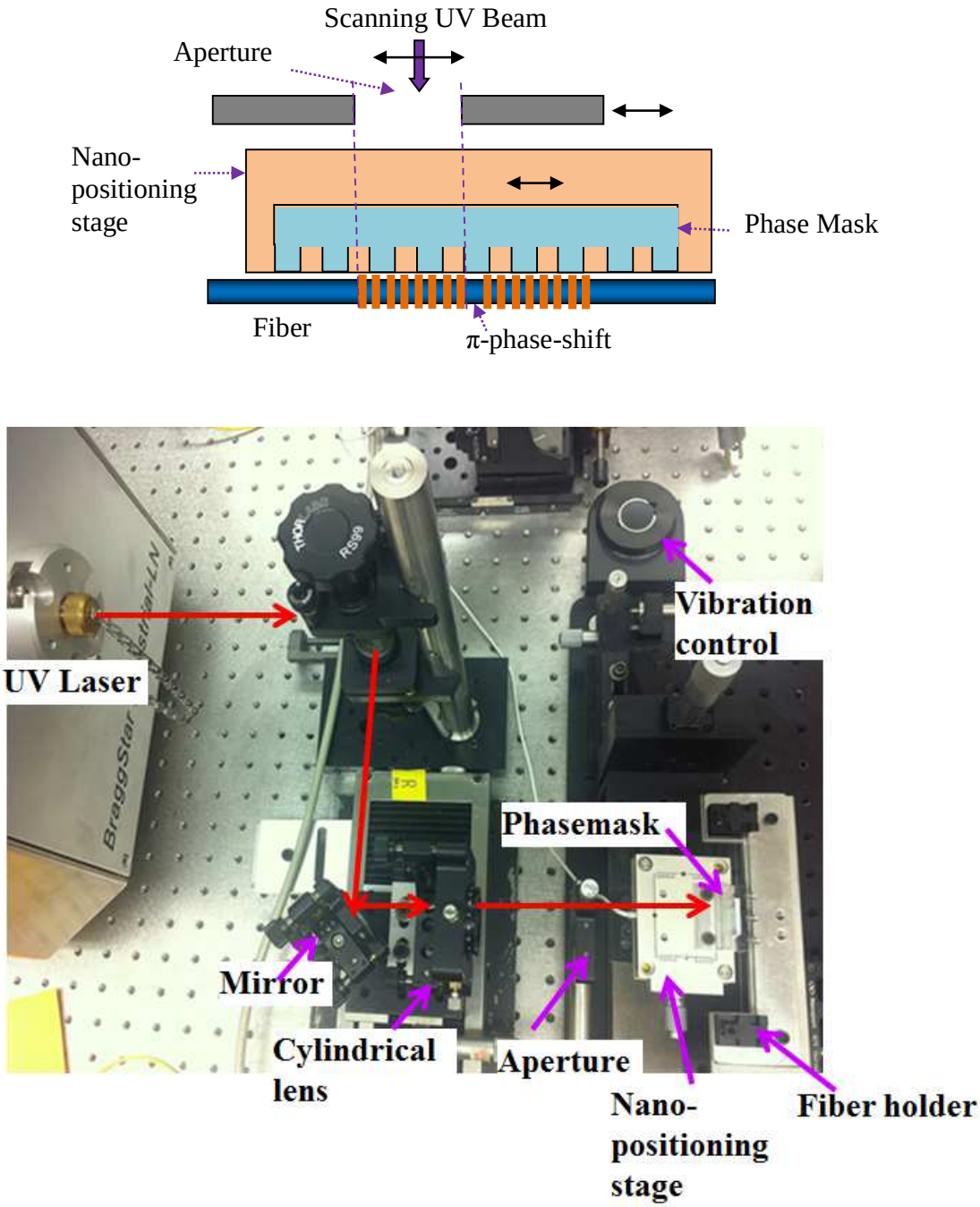

Figure 2.3: Schematic of πFBG fabrication using a scanning UV laser and a phase mask on a nano-positioning stage (Above). Actual setup showing optical pathway and components (Below).

Particular to this setup is the necessity of a half-wave plate. The manner in which this setup is constructed results in a horizontal laser beam with a vertical linear polarization

impinging upon a horizontal fiber. This alignment results a fabricated birefringence as will be discussed in Chapter 2.4. This is easily rectified by placing a half wave plate in the laser path at a 45° rotation angle to change the linear polarization of the laser by 90°.

2.4 Characterization of Fabricated πFBGs

There are several parameters to note when attempting to characterize a πFBG that will be used to detect ultrasonic emissions. First, the overall reflectivity of the grating is important, as the πFBG can be seen as an in-fiber FP cavity. As the reflectivity of the grating increases, so does the quality factor of the FP cavity. The maximum spectral slope of the πFBG also increases with reflectivity. This is measured during fabrication by using an optical spectrum analyzer (OSA) to measure the transmission spectrum of the πFBG as it is being written.

The width of the spectral notch of the πFBG is another key factor in determining the performance of the grating. The notch spectral width, along with the grating's reflectivity, determines the slope of the linear region used for the laser-intensity based demodulation used in this work. Unlike the reflectivity of the grating, the notch spectral width cannot be accurately measured by the OSA. This is because the OSA has a spectral resolution of 20 pm, while the spectral width of the notch varies in the range of 1~5 pm.

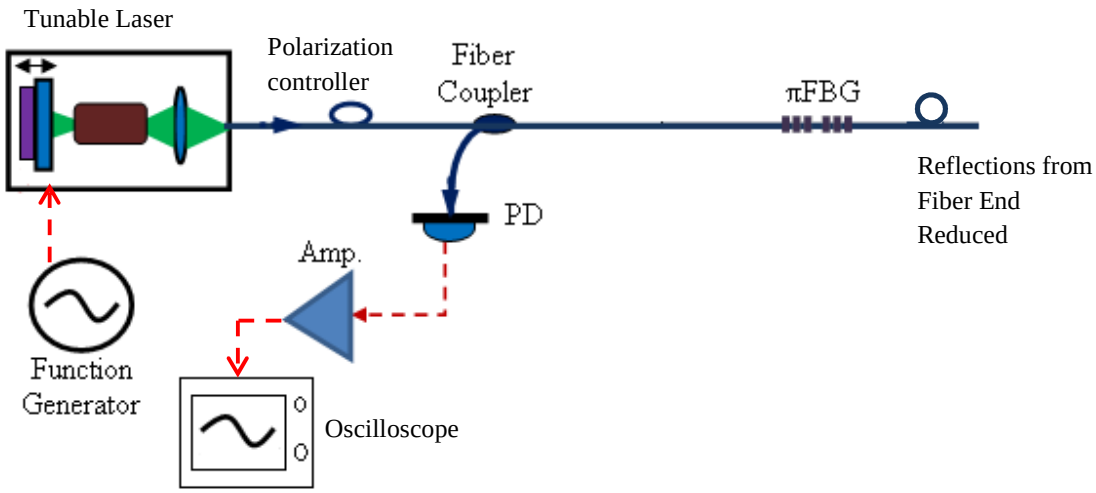

Figure 2.4: Schematic of setup used to characterize fabricated πFBGs.

To measure the width of a πFBG spectral notch after fabrication, a setup shown schematically in Fig. 2.4 is used. A narrow-linewidth tunable diode laser acts as the optical source. A periodic triangle wave signal is applied to the frequency modulation input of the tunable laser. This results in a linear sweeping of the laser wavelength that can be observed in the time domain via oscilloscope. By observing the reflection of the sweeping laser signal centered around the wavelength of the πFBG spectral notch, the width of the notch can be determined. This is done by measuring the change in the sweeping voltage over the width of the notch. The specifications of the laser used for this measurement state that for a PZT voltage range of 6 V, the laser wavelength can be modulated by 240 pm. This allows us to determine the width of the notch by applying

$$\Delta\lambda = \frac{240\ pm}{6\ V}\Delta V \tag{2.1}$$

where $\Delta\lambda$ is the change in wavelength for the given change in voltage, ΔV. The results of such a measurement are shown in Fig. 2.5. By using Eq. 2.1, we estimate the full width

at half maximum (FWHM) of the grating's spectral notch to be approximately 1.648 pm. It is important to note that this process was performed on the same demodulation setup for the experiments in this work as will be described in Chapter 3.

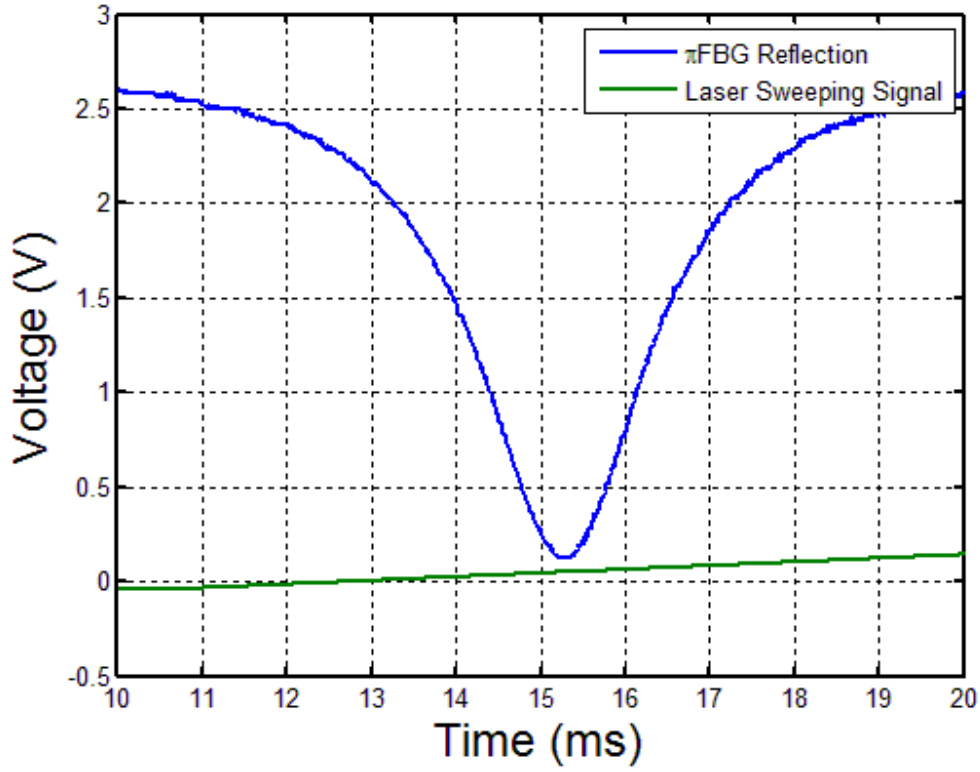

Figure 2.5: The reflected signal from a πFBG observed as the laser wavelength is swept across the spectral notch.

Finally, an important factor to consider for πFBGs is the birefringence of the grating. Since a grating's Bragg wavelength is dependent upon its effective refractive index, it becomes apparent that a birefringence in the cross section of the grating would result in multiple Bragg wavelengths depending upon the polarization of the light used to interrogate it. This effect, observed in Fig. 2.6, can be measured by the same methods used to measure the width of the πFBG spectral notch. In this case two spectral notches,

separated by approximately 7.68 pm, are observed by controlling the polarization of the laser to align at a 45° angle to the optical axes of the birefringence of the grating.

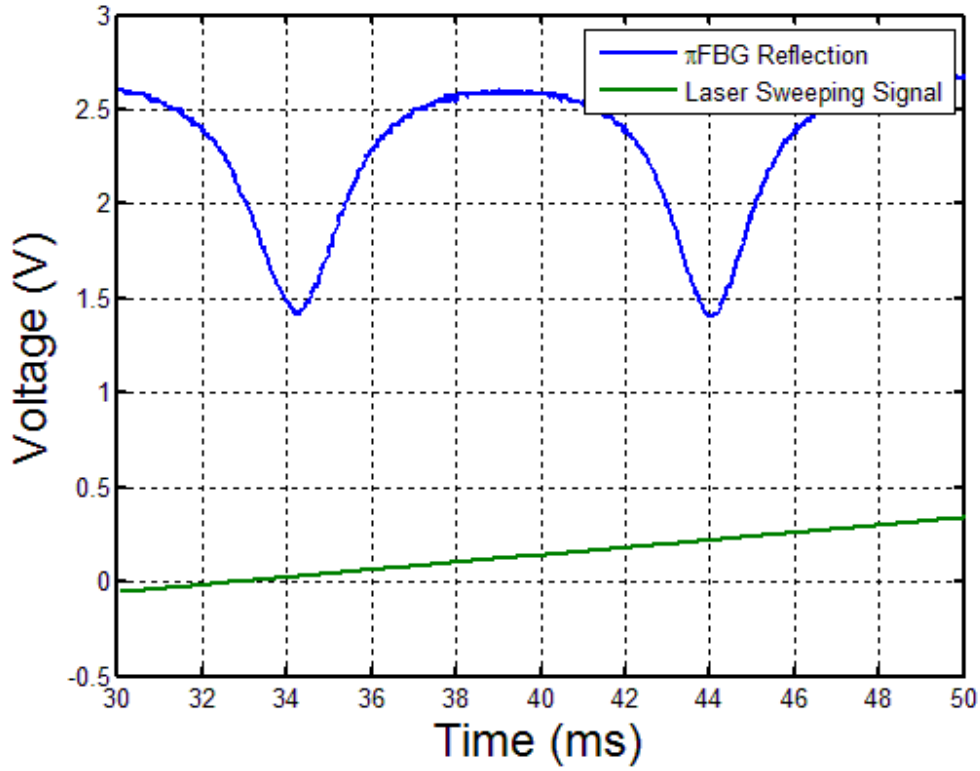

Figure 2.6: Two spectral notches of a πFBG are observed at different wavelengths due to birefringence.

Since the effects of birefringence on the πFBG's sensing capabilities can be controlled by simply controlling the polarization of the light source, it should be sufficient for this work to describe some of the primary sources of birefringence likely to be encountered during experimentation.

Due to the methods of the fabrication of standard single mode fiber, it is not perfectly circularly symmetric, which results in a relatively small inherent birefringence in all fiber used for this work.

The UV excimer laser used in grating fabrication can also induce a large birefringence in a fiber [24]. This can occur during FBG fabrication when such a laser impinges upon a fiber with a linear polarization that is perpendicular to the axial direction of the fiber. This effect occurs only in the Ge-doped core of the fiber, as it shows some slight inherent photosensitivity. Previous works have shown that the UV induced refractive index change in photosensitive fibers is highly dependent upon the polarization of the UV light [24].

Another form of birefringence occurs as the result of strain induced on the grating. Strain-induced birefringence is a result of the elasto-optic effect [25]. In the case of a semi-permanent strain, such as the bonding of a fiber to a surface via epoxy, it is possible to induce a large birefringence that should be considered as permanent as the strain causing it.

Chapter 3

Experimental Detection of Ultrasonic Waves

Since we now have the necessary methods to fabricate πFBG sensors and have provided enough useful information to analyze results of experimentation, we can begin to describe the experimentation of the work.

3.1 Demodulation Setup

First, we need to implement an experimental setup that will become the base for several experiments. This experimental setup is shown in Fig. 3.1. In order to accommodate a large wavelength range for use with various sensors at multiple wavelengths, we choose to use an external-cavity tunable-wavelength diode laser (Model 6262, Newport) with a linewidth of <300 kHz. This also gives us quick, precise control of the laser wavelength, and the ability to sweep the wavelength rapidly using the laser's built in PZT controlled fine tuning. After coupling this laser into standard SMF, a manual 3-paddle polarization controller is included. This polarization controller is necessary to ensure that the polarization of the laser is aligned with only one of the grating's axes of birefringence. A

fiber circulator is then included to direct the laser to the πFBG and to direct the reflected light from the πFBG to a photodetector. The signal may then be amplified in one of several ways, depending upon the specific experimental requirements. The πFBG itself is bonded onto a 24”x24”x0.05” aluminum plate via epoxy (M-Bond 200). The small thickness of the plate is to ensure that only the lowest order Lamb waves are excited for the frequency range used in this work. The plate serves as the ultrasonic wave transmission medium for all experiments and is therefore placed on noise isolation feet.

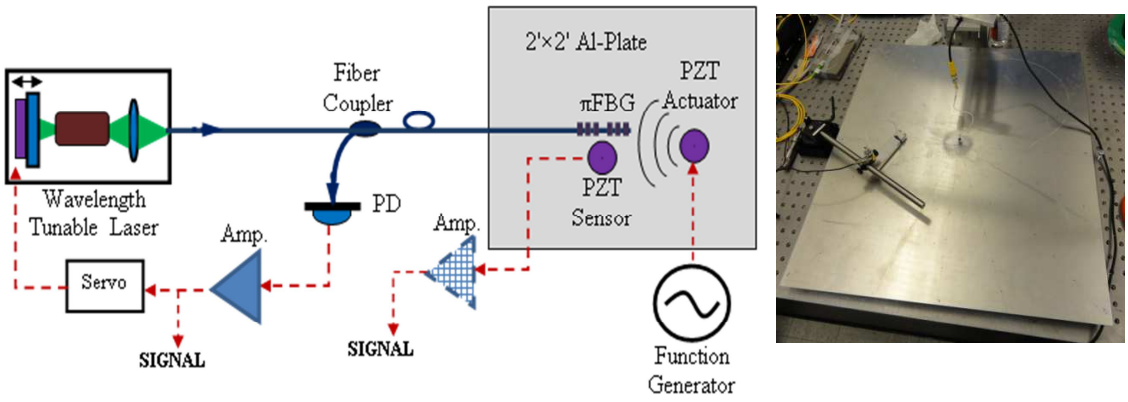

Figure 3.1: Schematic and picture of πFBG ultrasonic detection system (servo controller only included if needed).

3.2 πFBG Directivity Characterization

Directivity is an important parameter for ultrasonic sensors, describing the sensitivity of the sensor to ultrasonic waves impinging upon it from different directions. This experiment is to determine the directivity of a πFBG to impinging ultrasonic Lamb waves. We predict that sensitivity of the πFBG will be highest when the maximum strain of the impinging ultrasonic waves is aligned with the axial direction of the fiber for maximum modification of the grating period and refractive index.

3.2.1 Experimental Setup Specifics

We test this theory using the setup shown in Fig. 3.1 with the detection area shown schematically in Fig. 3.2. The πFBG sensor used is a commercially made grating.

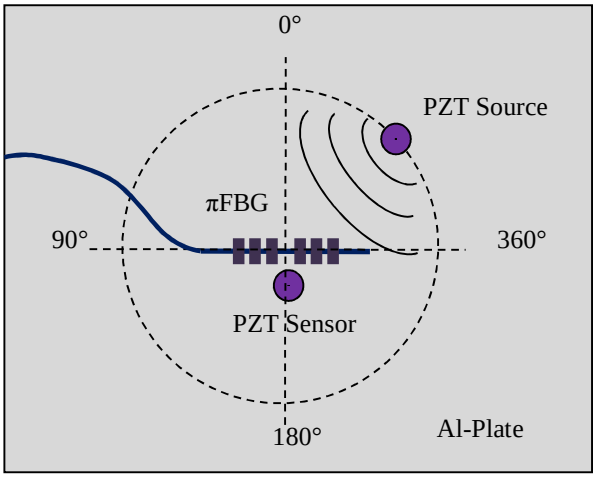

Figure 3.2: Schematic of plate setup and angles used in directivity experiment.

Two PZTs (HD50, Physical Acoustics Corp.) are used, one as a movable source and the other as a sensor mounted by epoxy (M-Bond 200) near the πFBG. Since these PZTs are circularly symmetric, we assume the sensors are omnidirectional. We then generated ultrasonic waves at various impinging angles to the grating, using the PZT sensor to characterize the response of the πFBG. The source PZT was driven by a function generator providing a 20 Vpp sinusoidal 3-cycle burst signal. The grating signal was amplified by a PZT amplifier (AE-2A, Physical Acoustics Corp.) set to 35 dB while the PZT sensor was not amplified.

3.2.2 Experimental Results

For the results of this experiment, the peak-to-peak voltage of the first wave packet observed is considered to be the signal amplitude. Using the first observed wave packet ensures that the signal is not a result of some reflection. The signal of the πFBG was then normalized by the signal amplitude of the PZT sensor.

The experiment was performed twice, with both experiments and their average being shown in Fig. 3.3. It is clear from these experiments that the directivity of the grating represents a cosine function of the impinging angle. This means that the sensor is most sensitive to ultrasonic waves aligned with the grating axis, and least sensitive to waves impinging perpendicular to the grating axis. This directivity is similar to what has been observed for regular FBG ultrasonic sensors [8].

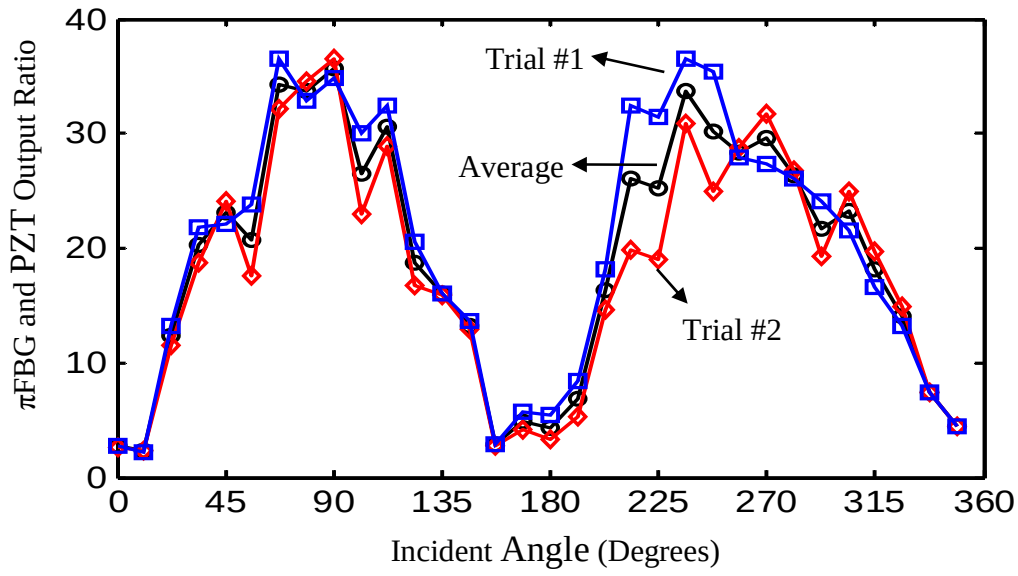

Figure 3.3: Numerical results showing the measured directivity results with respect to incident angle.

It is important to note that these results only characterize the directivity of the πFBG sensor for impinging lamb waves. Since a fairly thin plate is used, only the zero-order Lamb waves are excited for the frequency used in this experiment. Furthermore, since the asymmetric and symmetric zero-order Lamb wave modes propagate at different velocities, it is very likely that the first wave packet only consists of the zero-order symmetric mode Lamb waves.

3.3 Characterization with PZT Ultrasonic Source

In order to experimentally characterize the sensitivity of the πFBG sensor, it is necessary to perform an experiment using a PZT source generated ultrasonic wave, such as would be found in ultrasound testing. A PZT sensor placed near the grating can provide valuable characterization information for the πFBG since the response of PZT sensors is widely known.

It is important to note, however, that this experiment is meant to perform a preliminary investigation into the response of πFBGs. A head-to-head comparison of the overall performance of a πFBG sensor with a PZT sensor is not possible in this case because the two types of sensors are very different, a completely different demodulation technique is used, and there is no known figure of merit for directly comparing the sensitivity of these two sensors.

3.3.1 Experimental Setup Specifics

For this experiment, an 8 mm long πFBG with an approximate notch spectral width of 1.648 pm manufactured by the UV phase mask method mentioned in Chapter 2.3 is used.

A PZT sensor (R15α, Physical Acoustics Corp.) is placed near the πFBG, coupled by a small amount of glycerin and held in place by a light weight. The πFBG sensor was amplified by 40 dB after the photodetector by an ultrasonic amplifier (5676, Olympus). The PZT sensor was also amplified by an ultrasonic amplifier (AE-2A, Physical Acoustics Corp.) set to 35 dB amplification. The source PZT (HD50, Physical Acoustics Corp.) was placed approximately 2" away from the center of the grating in the axial direction. The PZT sensor was then adjusted slightly to ensure maximum coupling for the signal generated by the PZT source. The source PZT was powered by a 10 Vpp sinusoidal 3-cycle burst signal at a 20 Hz repetition rate. The low repetition rate is to ensure that the resonance of the previous wave packet has been damped sufficiently enough to not interfere with the measurement of the next packet.

The experiment was performed by altering the source's center frequency range from 150 kHz to 400 kHz in increments of 10 kHz, and taking data from each center frequency via oscilloscope.

3.3.2 Experimental Results

In order to characterize the results of the experiment, several parameters were chosen for measurement. The amplitude of the signal received by each sensor was chosen as the peak-to-peak voltage of the first wave packet received after the ultrasonic wave was emitted. This ensures that the signal measured is directly from the PZT source, and eliminates the possibility of a reflection constructively interfering with a wave packet from the source. The noise of the system was measured as the root-mean-square (RMS) value of the noise when the signal to the ultrasonic source was removed. Examples for

each set of raw data are shown for a 200 kHz signal in Fig. 3.4 for the πFBG signal, πFBG noise, the PZT sensor signal, and PZT sensor noise. The noise values were found to be approximately $N_{\pi FBG}$ = 17.4 mV_{rms}, and $N_{R15\alpha}$ = 1.3 mV_{rms}.

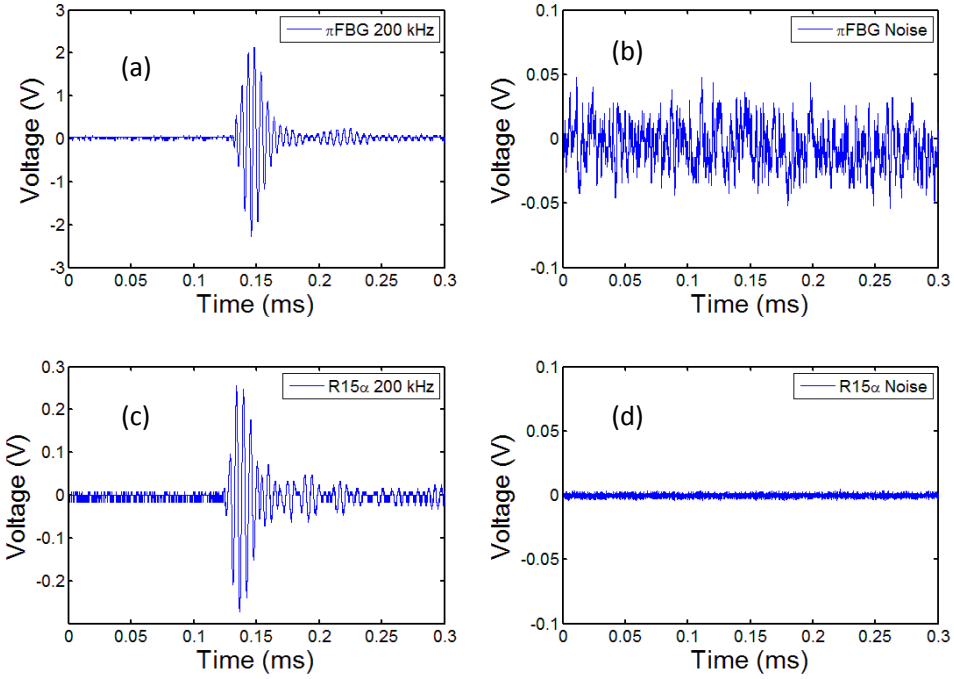

Figure 3.4: (a) Measured ultrasonic signal from the πFBG (b) Noise floor measured for the πFBG (c) Measured ultrasonic signal from the R15α PZT sensor (d) Noise floor measured for the R15α PZT sensor. The signals were obtained for the source PZT center frequency set to 200 kHz. The noise floors were obtained by removing the signal to the source PZT.

The signal-to-noise ratio (SNR) of each signal is then calculated as

$$SNR = 20log_{10}\left(\frac{V_s/\sqrt{2}}{RMS_n}\right) \tag{3.1}$$

where V_s is the peak-to-peak voltage of the first signal packet, and RMS_n is the RMS value of the noise. A plot of the SNR measured by this experiment as a function of frequency is shown in Fig. 3.5.

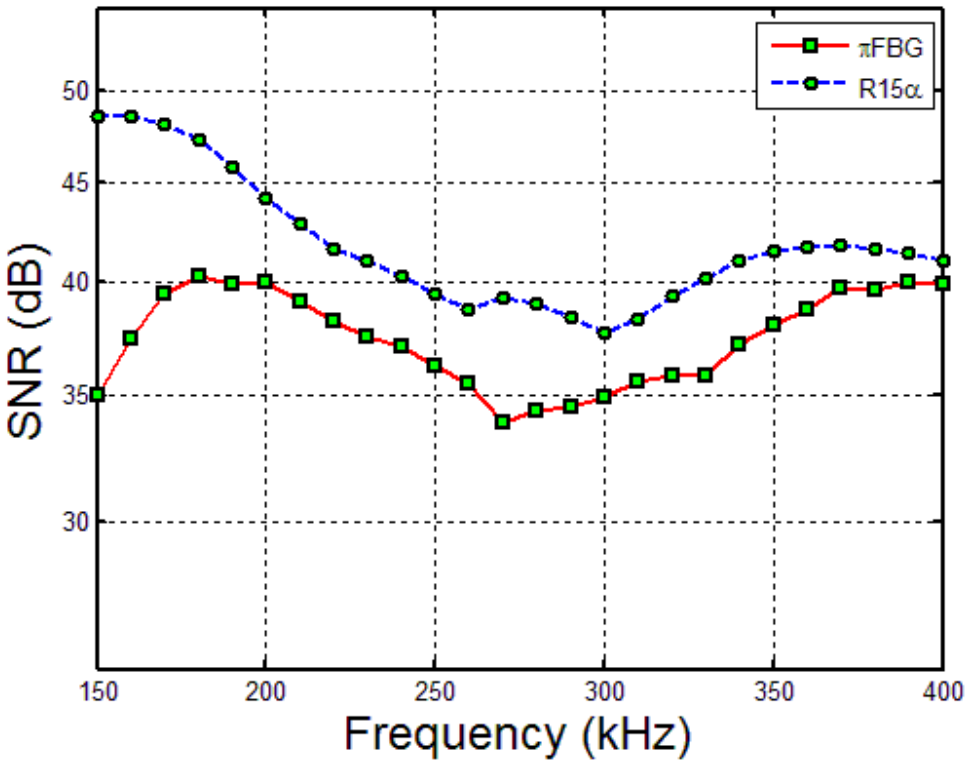

Figure 3.5: Measured Signal-to-Noise Ratio plotted for the ultrasonic source center frequency for the πFBG sensor and R15α PZT sensor.

From these results, it is apparent that for the particular setup in this experiment, the SNR of the PZT sensors outmatches the SNR of the πFBG by amounts varying from 14 dB to just 1 dB. It should be noted, however, that the components of this system may not be optimized to reflect the maximum SNR deliverable by a πFBG sensor. More analysis of the SNR of the πFBG demodulation system is required to understand these results, and is discussed in detail in Chapter 4.

3.4 Characterization with Pencil Lead Break Source

In addition to testing πFBGs with a controlled electronic source, it is important to also consider how the πFBG would perform when detecting random acoustic emissions generated by the formation of micro-cracks or other faults. A pencil lead break event is a simple way to simulate these acoustic emissions. This is done by breaking a piece of pencil lead on the surface of the detection medium.

3.4.1 Experimental Setup Specifics

This experiment uses the same πFBG and PZT sensor (R15α, Physical Acoustics) as the previous experiment, as well as the same aluminum plate. The πFBG again uses the same ultrasonic amplifier (5676, Olympus) while the PZT sensor uses the same ultrasonic amplifier (AE-2A, Physical Acoustics). The ultrasonic emission in this case is created by breaking a piece of 0.3 mm pencil lead approximately 3 mm long at a distance of about 6” from the sensors on the aluminum plate. Unfortunately, applying pressure on the pencil to break the lead creates a large strain on the aluminum plate. Since the πFBG sensor is highly sensitive to strain, there is a large spectral shift in the Bragg wavelength. In order to account for this, a high-speed servo controller (LB1005, Newport) is used to control the laser wavelength. This servo controller uses the low frequency output of the πFBG to adjust the tunable laser’s PZT controlled fine wavelength tuning. This keeps the wavelength of the laser locked to the linear portion of the spectral notch of the πFBG. In addition, the aluminum plate is placed directly on the flat surface of an optical table in order to reduce the magnitude of the strain created by applying pressure to the pencil lead.

3.4.2 Experimental Results

The goal of this experiment is ultimately to characterize the frequency response of a πFBG sensor to a random amplitude broadband ultrasonic acoustic emission. In addition, the SNR of this experiment should vary widely based on the random amplitude of the ultrasonic signal, but the SNR comparison between the two sensors for the same source signal would still be meaningful. The normalized frequency responses within the detection range for two of these experiments are plotted in Fig. 3.6a and Fig. 3.6b. As is expected, the πFBG frequency response displays the characteristics of a broadband signal, while the PZT sensor has various sensitive peaks in its frequency response corresponding to its resonance frequencies.

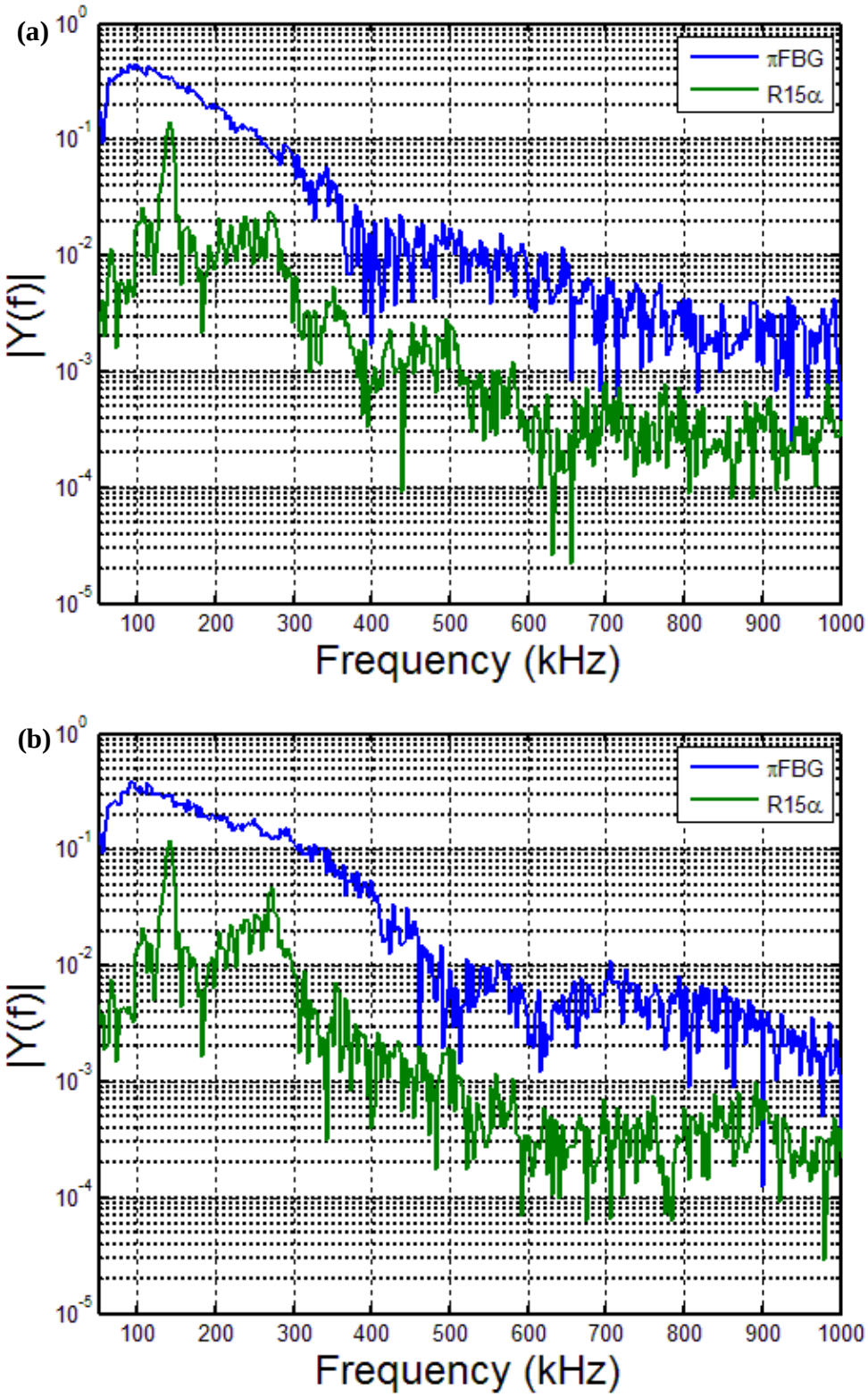

Figure 3.6: (a) ,(b) The frequency response of two separate instances of a pencil lead break experiment, obtained by taking the single sided magnitude of the normalized Fourier transform of each signal over the detection range of 50 kHz to 1 MHz.

Chapter 4

Noise Analysis

Now that experimentation has been performed for ultrasonic detection using πFBGs, it becomes important to analyze the noise performance of the demodulation system. This is because the sensitivity of the system, as well as its dynamic sensing range, is ultimately determined by the level of noise. The goal of this chapter is to provide this analysis theoretically, and to use this information to explain the noise encountered in the experimental results. This will allow us to further optimize the performance of the πFBG sensor system for highly sensitive detection of ultrasonic emissions.

4.1 Noise Sources

To begin this analysis, we must consider which sources of noise to analyze. The demodulation system consists of several optical and electrical components with their own noise contributions. Since we are interested in the noise performance of the πFBG in particular, only the noise sources of the demodulation system up to the photodetector are considered. The electronic amplifiers are ignored for this analysis. This leaves two primary sources of noise to be analyzed; the narrow-linewidth laser and the photodetector.

In order to analyze the noise of the system, we must first create a signal with which to characterize the noise with. Consider the case where a narrow-linewidth laser of power $2P_0$ has its wavelength locked to a point on the spectral notch of a πFBG sensor having 50% reflectivity. The ultrasonic wave is then characterized as having a frequency, Ω. Assuming the impinging ultrasonic wave also induces a spectral shift in the πFBG, the laser power reflected by the grating, P_{ref}, is then given by

$$P_{ref} = P_0 + k\delta\nu \cos \Omega t \tag{4.1}$$

where $\delta\nu$ is the amplitude of the spectral shift in the πFBG reflection spectrum and k is the slope of the πFBG reflection spectrum in the frequency domain in units of 1/Hz. The cosine term describes the effect of ultrasonic wave on the πFBG and is considered to be the signal for this analysis.

Now that we have Eq. 4.1 to describe the laser power reflected from the grating, we can use it to describe the power of the signal seen by the photodetector. The root-mean-square (RMS) value of the output signal of the photodetector is given by

$$\overline{i_S^2(t)} = \frac{1}{2}\Re^2 P_0^2 k^2 \delta\nu^2 \tag{4.2}$$

where $\Re$ is the responsivity of the photodetector as defined by the current generated by impinging optical power given in units of A/W.

The photodetector itself introduces two types of noise to the signal, shot noise and thermal noise. Shot noise comes from the quantum nature of light. Any light source can

be considered to consist of a stream of photons which exhibits detectibly non-constant flow. The shot noise of the photodetector comes from the fluctuations in the flow of photons, and the RMS value of it is given by[26]

$$\overline{i_{SN}^2} = 2e\Re P_0 \Delta f \tag{4.3}$$

where e is the elementary charge of an electron, and Δf is the bandwidth of the detection electronics. The thermal noise of the photodetector is due to the thermal drift of electrons and its RMS value is given by[26]

$$\overline{i_{th}^2} = \left(\frac{4k_B T}{R}\right)\Delta f \tag{4.4}$$

where k_B is the Boltzmann constant, T is temperature in degrees Kelvin, and R is the input impedance of the detection electronics.

Now we must consider the noise created by the narrow-linewidth laser and by its interaction with the πFBG. The two primary noise sources to consider from the laser are the relative intensity noise (RIN) and the frequency noise. These noise sources describe the fluctuations in laser intensity and laser frequency respectively.

The RIN of an external-cavity tunable-wavelength diode laser as used in this work is caused by multiple factors. Thermal fluctuations in the gain medium of the laser, vibration of the optical cavity, and several quantum factors all contribute to the RIN. For this analysis we consider the RIN of the narrow-linewidth laser to be a white noise over the detection bandwidth with its power spectral density (PSD) S_{RIN} given in units of 1/Hz

or dB/Hz. All PSDs in this work are considered as single-sided. The RMS power of the noise after the photodetector that corresponds to the laser RIN is given as

$$\overline{i_{RIN}^2} = \Re^2 P_0^2 S_{RIN} \Delta f. \tag{4.5}$$

The last noise source to consider is the laser frequency noise. The laser frequency noise contributes to the overall system noise primarily because of the attributes of the πFBG. Consider that for demodulation, the laser is locked to a linear region of the πFBG's reflection spectrum. The large slope of this region effectively creates a frequency discriminator whereby fluctuations in the laser wavelength result in fluctuations of the optical power reflected by the πFBG. The PSD of the laser's frequency noise, $S_{\Delta\nu}(f)$, depends on the characteristics of the laser. For a continuous wave laser with a Lorentzian lineshape, the frequency noise is a white noise and its PSD is related to the laser linewidth by [27]

$$S_{\Delta\nu}(f) = \frac{\Delta\nu}{\pi} \tag{4.6}$$

where $\Delta\nu$ is the FWHM of the laser linewidth. The RMS power of this noise after the photodetector can then be approximated by

$$\overline{i_{\Delta\nu}^2} = \Re^2 P_0^2 k^2 S_{\Delta\nu}(f) \Delta f. \tag{4.7}$$

By substituting Eq. 4.6 into Eq. 4.7, we get

$$\overline{l_{\Delta\nu}^2} = \frac{1}{\pi}\Re^2 P_0^2 k^2 \Delta\nu \Delta f. \tag{4.8}$$

4.2 Analysis of Signal-to-Noise Ratio

Now that we have equations approximating the various major sources of noise for the demodulation system, an analysis can be performed to characterize the system's overall noise levels to find the system's SNR. First, the RMS power of the overall noise is given simply by the sum of the noise sources as

$$\begin{aligned}\overline{l_N^2} &= \overline{l_{SN}^2} + \overline{l_{th}^2} + \overline{l_{RIN}^2} + \overline{l_{\Delta\nu}^2} \\ &= \left(2e\Re P_0 + \frac{4k_B T}{R} + \Re^2 P_0^2 S_{RIN} + \frac{1}{\pi}\Re^2 P_0^2 k^2 \Delta\nu\right)\Delta f.\end{aligned} \tag{4.9}$$

Using Eq. 4.9 and Eq. 4.2, which describes the power of the signal after the photodetector, we can give the approximate SNR of the system as

$$SNR = \frac{\overline{l_s^2}}{\overline{l_N^2}} = \frac{\frac{1}{2}\Re^2 P_0^2 k^2 \delta\nu^2}{\left(2e\Re P_0 + \frac{4k_B T}{R} + \Re^2 P_0^2 S_{RIN} + \frac{1}{\pi}\Re^2 P_0^2 k^2 \Delta\nu\right)\Delta f} \tag{4.10}$$

The approximation of the system SNR given by Eq. 4.10 can now be used to determine the role each noise source has in the overall SNR of the system. This can be done by choosing some typical values for the parameters of the system. As an example of a typical system, assume the values in Table 4.1.

P_0	5 mW
$\Re$	0.95 A/W
R	2 kΩ
T	300 K
S_{RIN}	150 dB/Hz

Table 4.1: Typical parameters for an example system

The PSDs of the noises after the photodetector are then approximated using their respective equations above as: PSD_{SN} = -208 dB/Hz, PSD_{th} = -230 dB/Hz, and PSD_{RIN} = -196 dB/Hz. The laser RIN alone is more than 10 dB greater than the photodetector shot noise and more than 30 dB greater than the photodetector thermal noise. It is clear from these approximations that the noise sources from the laser are dominant.

Given the dominance of the laser noise sources, this analysis now shifts to focus primarily on the laser RIN and laser frequency noise. By ignoring the photodetector shot noise and thermal noise and considering only the noise sources of the laser, the SNR of the system becomes

$$SNR = \frac{\frac{1}{2}k^2\delta\nu^2}{\left(S_{RIN} + \frac{1}{\pi}k^2\Delta\nu\right)\Delta f} \tag{4.11}$$

From Eq. 4.11 it becomes clear that the SNR of the system is independent of optical power. Since the frequency noise actually leads to noise in the reflected optical power, we can define the PSD of an equivalent RIN, S_{LW}, related to the frequency noise as

$$S_{LW} = \frac{1}{\pi} k^2 \Delta\nu \tag{4.12}$$

Finally, the SNR of the system becomes

$$SNR = \frac{\frac{1}{2} k^2 \delta\nu^2}{(S_{RIN} + S_{LW})\Delta f} \tag{4.13}$$

4.3 Characterization of System Parameters

The SNR of the demodulation system has now been described by Eq. 4.13. This was arrived at by first describing the noise sources as characterized by a theoretical signal given in Eq. 4.1. The laser noise sources were then shown to be dominant when compared to the noises from the photodetector. Now the parameters of the system such as the laser linewidth and πFBG will be considered.

As shown in Chapter 4.1 and 4.2, the frequency noise of the laser can be approximated as a RIN with a PSD of S_{LW} because of the effect of the slope of the reflection spectrum of the πFBG acting as a frequency discriminator. This leads to S_{LW} being proportional to the square of this slope. Since the laser RIN is independent of the πFBG, S_{LW} will become the dominant noise with the narrowing of the πFBG spectral notch.

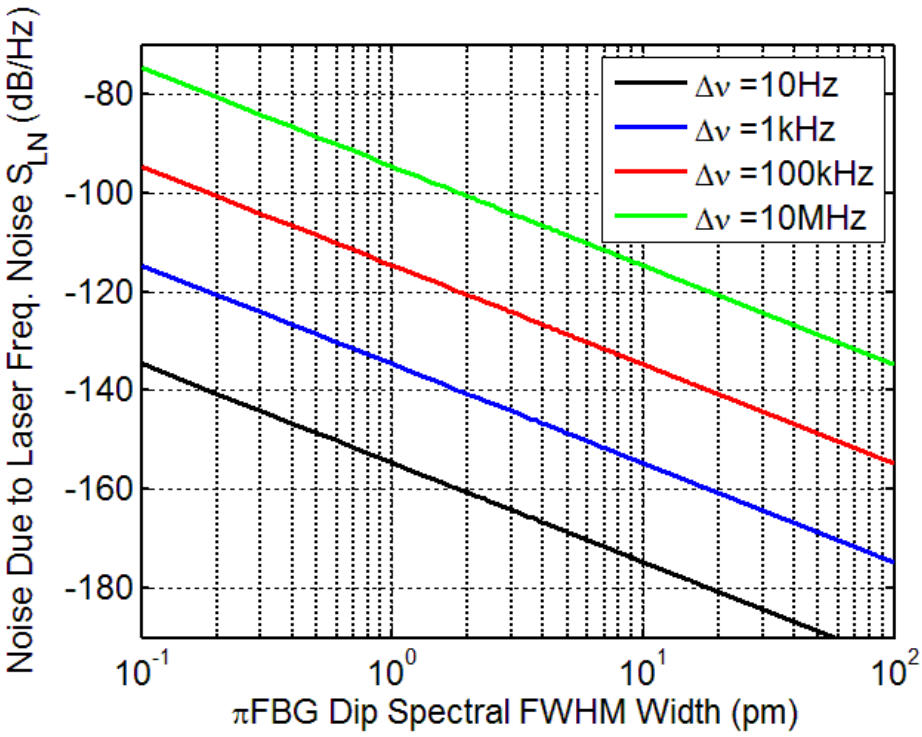

Figure 4.1: The effective RIN caused by the laser frequency noise plotted as a function of the width of the πFBG spectral notch for several laser linewidths.

To compare the laser RIN with the RIN caused by the laser frequency noise, the S_{LW} is plotted with respect to the width of the πFBG spectral notch for several laser linewidths in Fig. 4.1. From this graph we are able to see clearly that as the width of the πFBG's spectral notch decreases, S_{LW} increases and eventually becomes the dominant noise for a laser with a given RIN. We can also use such a graph to determine the appropriate width of a πFBG's spectral notch to use for a particular laser. For instance, given a laser RIN of -140 dB/Hz and a laser linewidth of 100 kHz, S_{LW} begins to dominate at a πFBG spectral notch width of 20 pm.

Furthermore, the theoretical SNR of a system can be easily characterized by plotting the theoretical SNR of the system as a function of the width of the πFBG spectral notch such

as shown in Fig. 4.2. Here, the SNR of the system for an arbitrary signal causing a wavelength shift of 0.03 pm in the πFBG reflection spectrum is plotted as a function of the width of the πFBG spectral notch for several laser linewidths. A graph such as this is very helpful in determining a theoretical SNR given the specific parameters of the setup. As it can be seen from Fig. 4.2, the FWHM of the πFBG's spectral notch has a limit on the improvement of the SNR of the system based on the laser's linewidth.

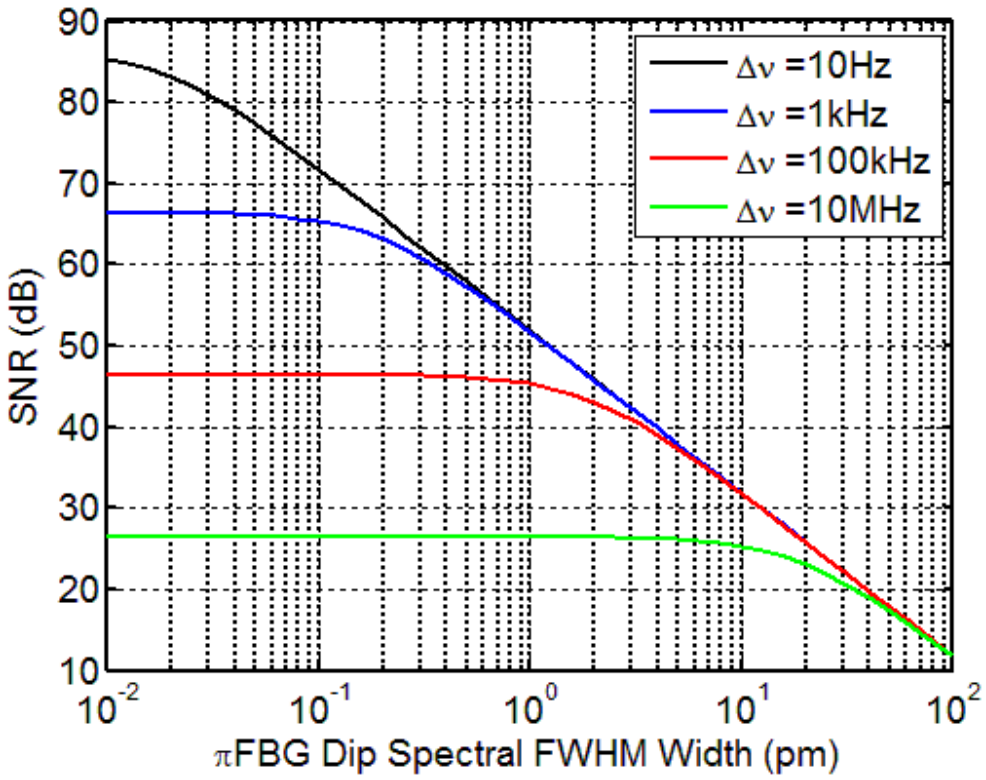

Figure 4.2: The theoretical SNR of the demodulation system for an arbitrary signal causing a spectral shift of 0.3 pm plotted as a function of the FWHM of the πFBG spectral notch for several laser linewidths.

Chapter 5

Conclusion

5.1 Summary

This thesis summarizes the introductory work into the experimental investigation of ultrasonic acoustic emission detection using πFBG sensors.

First, the motivation of the work is discussed along with a minimum of necessary theoretical background to understand the experimentation. Then, a commonly known method of normal FBG fabrication using a UV phase mask is introduced. Two methods of πFBG fabrication are discussed with a UV phase mask method being selected for the production of πFBGs for this work. The parameters and methods for characterizing a fabricated πFBG are discussed.

The experimentation of this work is then described in detail. A demodulation setup satisfying the requirements of this work is implemented. The directivity of a πFBG sensor is found to follow a cosine function of the impinging angle of an ultrasonic wave. In a demonstration of the sensitivity of the πFBG for detecting ultrasonic waves generated by a PZT source, the πFBG sensor is found to be capable of sensitive measurement of ultrasonic waves. Another experiment displaying the frequency

response of the πFBG to a broadband acoustic emission shows the πFBG to have low frequency dependence when compared to a PZT sensor.

The noise of the system is then theoretically analyzed to provide background into the SNR of the demodulation setup used for this work. The noise sources are identified and it is shown that the laser noise sources are dominant. Furthermore, the laser frequency noise is shown to become the dominant noise source depending upon the narrowness of the FWHM of the πFBG's spectral notch. Finally, the effects of the parameters of certain components on the SNR of the system are displayed graphically.

5.2 Future Work

There are several possibilities for future investigations of πFBG sensors for ultrasonic emission detection that would directly follow this work. The optimization of the πFBG SNR for a true comparison of sensitivity against a PZT sensor is one such line of investigation. A feature of πFBG detection that was not thoroughly investigated for this work was the effect of birefringence upon ultrasonic emission detection. This is because for all above experimentation, the results are only observed for one polarization of the πFBG. Another avenue of research is to experimentally demonstrate ultrasonic detection using a multiplexed πFBG sensor. Finally, more work is needed in developing a practical demodulation system. The system used in this work requires a complicated tunable narrow linewidth laser with a wide wavelength range in order to track the large wavelength shifts caused by quasi-dynamic strain on the πFBG sensor.

References

[1] I. M. Perez, *et al.*, "Acoustic emission detection using fiber Bragg gratings," in *SPIE's 8th Annual International Symposium on Smart Structures and Materials*, 2001, pp. 209-215.

[2] H. Tsuda, "Ultrasound and damage detection in CFRP using fiber Bragg grating sensors," *Composites science and technology*, vol. 66, pp. 676-683, 2006.

[3] D. C. Betz, *et al.*, "Structural damage location with fiber Bragg grating rosettes and Lamb waves," *Structural health monitoring*, vol. 6, pp. 299-308, 2007.

[4] G. Wild and S. Hinckley, "Acousto-ultrasonic optical fiber sensors: Overview and state-of-the-art," *Sensors Journal, IEEE*, vol. 8, pp. 1184-1193, 2008.

[5] M. De Vries, *et al.*, "Performance of embedded short-gage-length optical fiber sensors in a fatigue-loaded reinforced concrete specimen," *Smart Materials and Structures*, vol. 4, p. A107, 1999.

[6] P. Moyo, *et al.*, "Development of fiber Bragg grating sensors for monitoring civil infrastructure," *Engineering structures*, vol. 27, pp. 1828-1834, 2005.

[7] K. Wood, *et al.*, "Fiber optic sensors for health monitoring of morphing airframes: I. Bragg grating strain and temperature sensor," *Smart Materials and Structures,* vol. 9, p. 163, 2000.

[8] D. C. Betz, *et al.*, "Acousto-ultrasonic sensing using fiber Bragg gratings," *Smart Materials and Structures,* vol. 12, p. 122, 2003.

[9] N. Fisher, *et al.*, "Ultrasonic hydrophone based on short in-fiber Bragg gratings," *Applied optics,* vol. 37, pp. 8120-8128, 1998.

[10] P. Fomitchov and S. Krishnaswamy, "Response of a fiber Bragg grating ultrasonic sensor," *Optical Engineering,* vol. 42, pp. 956-963, 2003.

[11] A. Minardo, *et al.*, "Response of fiber Bragg gratings to longitudinal ultrasonic waves," *Ultrasonics, Ferroelectrics and Frequency Control, IEEE Transactions on,* vol. 52, pp. 304-312, 2005.

[12] J. R. Lee, *et al.*, "Impact wave and damage detections using a strain-free fiber Bragg grating ultrasonic receiver," *NDT & E International,* vol. 40, pp. 85-93, 2007.

[13] J. R. Lee, *et al.*, "Single-mode fibre optic Bragg grating sensing on the base of birefringence in surface-mounting and embedding applications," *Optics & Laser Technology,* vol. 39, pp. 157-164, 2007.

[14] D. Gatti, *et al.*, "Fiber strain sensor based on a π-phase-shifted Bragg grating and the Pound-Drever-Hall technique," *Optics express,* vol. 16, pp. 1945-1950, 2008.

[15] A. Rosenthal, *et al.*, "High-sensitivity compact ultrasonic detector based on a pi-phase-shifted fiber Bragg grating," *Optics letters,* vol. 36, pp. 1833-1835, 2011.

[16] L. Wei and J. W. Y. Lit, "Phase-shifted Bragg grating filters with symmetrical structures," *Lightwave Technology, Journal of,* vol. 15, pp. 1405-1410, 1997.

[17] E. Chehura, *et al.*, "Pressure measurements on aircraft wing using phase-shifted fibre Bragg grating sensors," in *20th International Conference on Optical Fibre Sensors*, 2009, pp. 750334-750334-4.

[18] T. Erdogan, "Fiber grating spectra," *Lightwave Technology, Journal of,* vol. 15, pp. 1277-1294, 1997.

[19] G. Hocker, "Fiber-optic sensing of pressure and temperature," *Applied optics,* vol. 18, pp. 1445-1448, 1979.

[20] Y. J. Rao, "In-fibre Bragg grating sensors," *Measurement science and technology,* vol. 8, p. 355, 1999.

[21] K. Hill, *et al.*, "Bragg gratings fabricated in monomode photosensitive optical fiber by UV exposure through a phase mask," *Applied Physics Letters,* vol. 62, pp. 1035-1037, 1993.

[22] K. Hill, *et al.*, "Photosensitivity in optical fiber waveguides: Application to reflection filter fabrication," *Applied Physics Letters,* vol. 32, pp. 647-649, 1978.

[23] J. Albert, *et al.*, "Photosensitivity in Ge-doped silica optical waveguides and fibers with 193-nm light from an ArF excimer laser," *Optics letters,* vol. 19, pp. 387-389, 1994.

[24] T. Erdogan and V. Mizrahi, "Characterization of UV-induced birefringence in photosensitive Ge-doped silica optical fibers," *JOSA B,* vol. 11, pp. 2100-2105, 1994.

[25] A. Smith, "Birefringence induced by bends and twists in single-mode optical fiber," *Applied optics,* vol. 19, pp. 2606-2611, 1980.

[26] G. Bjorklund, *et al.*, "Frequency modulation (FM) spectroscopy," *Applied Physics B: Lasers and Optics,* vol. 32, pp. 145-152, 1983.

[27] G. Di Domenico, *et al.*, "Simple approach to the relation between laser frequency noise and laser line shape," *Applied optics,* vol. 49, pp. 4801-4807, 2010.